El Mayor-Cucapah (Mw 7.2) earthquake: early near-field postseismic deformation from InSAR and GPS observations

Alejandro Gonzalez-Ortega[1], Yuri Fialko[2], David Sandwell[2], F. Alejandro Nava-Pichardo[1], John Fletcher[1], Javier Gonzalez-Garcia[1], Brad Lipovsky[3,4], Michael Floyd[3,5] and Gareth Funning[3].

[1]Centro de Investigación Científica y de Educación Superior de Ensenada, B.C., División de Ciencias de la Tierra. Carretera Ensenada-Tijuana No. 3918, Zona Playitas, Ensenada, Baja California, 22860. México.

[2]Institute of Geophysics and Planetary Physics, Scripps Institution of Oceanography, University of California, San Diego, 9500 Gilman Drive, La Jolla, California, 92093-0225. USA.

[3]Department of Earth Sciences, University of California, Riverside, 900 University Ave. Riverside, California, 92521. USA.

[4]Now at School of Earth Sciences, Department of Geophysics, Stanford University. 397 Panama Mall. Stanford, California, 94305. USA.

[5]Now at Department of Earth, Atmospheric and Planetary Sciences, Massachusetts Institute of Technology. 77 Massachusetts Avenue, Cambridge, Massachusetts, 02142. USA.

This article has been accepted for publication and undergone full peer review but has not been through the copyediting, typesetting, pagination and proofreading process which may lead to differences between this version and the Version of Record. Please cite this article as doi: 10.1002/2013JB010193

Abstract

El Mayor-Cucapah earthquake occurred on April 4, 2010, in northeastern Baja California just south of the USA-Mexico border. The earthquake ruptured several previously mapped faults, as well as some unidentified ones, including the Pescadores, Borrego, Paso Inferior and Paso Superior faults in the Sierra Cucapah, and the Indiviso fault in the Mexicali Valley and Colorado River Delta. We conducted several Global Position System (GPS) campaign surveys of pre-existing and newly established benchmarks within 30 km of the earthquake rupture. Most of the benchmarks were occupied within days after the earthquake, allowing us to capture the very early postseismic transient motions. The GPS data show postseismic displacements in the same direction as the coseismic displacements; time series indicate a gradual decay in postseismic velocities with characteristic time scales of 66±9 days and 20±3 days, assuming exponential and logarithmic decay, respectively. We also analyzed Interferometric Synthetic Aperture Radar (InSAR) data from the Envisat and ALOS satellites. The main deformation features seen in the line-of-sight (LOS) displacement maps indicate subsidence concentrated in the southern and northern parts of the main rupture, in particular at the Indiviso fault, at the Laguna Salada basin, and at the Paso Superior fault. We show that the near-field GPS and InSAR observations over a time period of 5 months after the earthquake can be explained by a combination of afterslip, fault zone contraction, and a possible minor contribution of poroelastic rebound. Far-field data require an additional mechanism, most likely viscoelastic relaxation in the ductile substrate.

1. Introduction

The M_w 7.2 El Mayor-Cucapah earthquake occurred on April 4, 2010 just south of the US-Mexico Border. It caused serious damage in Mexicali City and in the entire Mexicali Valley, and was felt at distances over 200 km in northern Baja California, Mexico, and southern California, USA. The earthquake epicenter (31.13 N, 115.30 W; GCMT, www.globalcmt.org) is located within the boundary region between the North American and Pacific plates, which features a series of northwest trending transform faults parallel to, and contiguous to, strands of the San Andreas fault system in the Salton Trough (Figure 1). The mainshock rupture involved normal faulting as well as right-lateral strike-slip faulting [*Hauksson et al.*, 2010]. The surface rupture propagated along the previously known Pescadores and Borrego faults [*Fletcher and Spelz*, 2009] within the Sierra Cucapah, and along the Indiviso fault, inferred from InSAR imagery [*Fialko et al*., 2010; *Fielding et al.*, 2010; *Wei et al*., 2011a] and subsequently identified in the field on the sedimentary deposit of the Colorado River delta. The earthquake involved a 120 km-long NW-SE trending rupture that traversed two distinct geomorphologic and structural domains, extending from the town of Indiviso at the northern tip of the Gulf of California (hereafter referred to as the 'Delta domain'), and northwestward through the Sierra Cucapah to the international USA-Mexico border (the 'Sierra domain'). Field measured displacements mapped along the Pescadores fault involve 2.5 m of predominantly strike-slip character, and up to 4 m of oblique slip along the Borrego fault in the northern Sierra Cucapah [*Fletcher et al.*, 2013]. The rupture process was complex: it propagated through a network of known faults, as well as previously unmapped faults, like the Paso Inferior and Paso Superior faults which featured low-angle detachments activated during the earthquake [*Fletcher et al.*, 2013; *Oskin et al.*, 2012]. Also, the earthquake triggered slip on multiple faults strands in southern California [*Rymer et al.*, 2011; *Wei et al.*, 2011b]. The aftershock sequence extended in both directions from the

epicenter, to the northern tip of the Gulf of California and to the USA-Mexico border, defining a seismogenic zone extending to depth of ~10 km [*Castro et al.,* 2011].

Initially, space geodetic data, in particular, Interferometric Synthetic Aperture Radar (InSAR), and pixel offsets from optical imagery revealed a relatively straight continuous fault trace with maximum offsets of the order of 3 to 4 meters. Thereafter, inversions of geodetic and seismic data and precise aftershock locations indicated that the fault geometry is quite complicated below the surface, with significant along-strike variations in the fault dip angle, from an eastward dip in the Sierra domain, to a westward dip in the Delta domain, and suggested that the rupture was triggered by a normal faulting event on a fault plane of yet another orientation [*Hauksson et al.,* 2010; *Fialko et al*., 2010; *Wei et al.,* 2011a].

We conducted campaign GPS measurements starting from one day to one week after the El Mayor-Cucapah earthquake. The survey was carried out in the eastern and southern parts of the main rupture in Mexicali Valley, where previously installed GPS benchmarks were available; and in the northwest, in the Laguna Salada basin, where six new benchmarks were established. Measurements from 19 sites in Baja California and 20 permanent GPS stations in California, allowed us to obtain the coseismic and the very early postseismic displacements. The maximum horizontal coseismic displacement is 1.160±0.016 m, in the N137ºE direction, at campaign site La Puerta (LPUR) ~8 km from the epicenter in the southeastern part of the Sierra Cucapah, and the maximum vertical displacement is -0.636±0.036 m at site VM15 near the town of Durango, where liquefaction and ground failure caused severe damage to agricultural areas throughout the Mexicali Valley (Figure 1).

Geodetic observations indicate that the rate of postseismic deformation decays with time, and the maximum amplitude of postseismic displacements is typically one order of magnitude smaller than the coseismic ones [e.g., *Savage and Svarc*, 1997; *Jacobs et al.,* 2002; *Feigl and Thatcher*, 2006]. The observed postseismic transients exhibit time scales

ranging from days to months and years, depending on the distance to the main rupture. Physical mechanisms proposed to explain the transient deformation include: poroelastic rebound in the fluid-saturated crust; afterslip (continued aseismic slip) on the fault plane and/or its deep extension; and viscoelastic relaxation in the lower crust and upper mantle [e.g. *Burgmann and Dresen*, 2008; *Barbot and Fialko*, 2010]. These mechanisms may be operating individually or in combination [*Pollitz et al.*, 2001; *Jonsson et al.*, 2003; *Fialko*, 2004a; *Hearn et al.*, 2009; *Barbot et al.*, 2009].

Some assessment of the relative importance of different postseismic mechanisms would contribute to our understanding of the mechanical behavior of the lithosphere. In addition, identifying a dominant mechanism of postseismic deformation might help forecast the evolution of stress following large earthquakes for seismic hazard analysis. This is particularly important given that the earthquake occurred in an area just to the south of large population centers on both sides of the Mexico-USA (California) border and the Greater Los Angeles region further north.

In this study, we examine the postseismic deformation in the near-field following the 2010 El Mayor-Cucapah earthquake, using InSAR data from the Envisat and ALOS satellites from the first 5 months, and GPS data from the first 750 days after the event. We perform joint inversions of InSAR and GPS data spanning the first 5 months after the event for the best-fitting model that accounts for afterslip, volume changes in the fault zone, and poro-elasticity.

2. Data acquisition and processing

The GPS data used to calculate the interseismic crustal velocity model for northern Baja California were collected by a number of collaborating institutions since the early 1990's, including, the Salton Trough Riverside County group [*Bennett et al.*, 1996],

University of Miami [*Dixon et al.*, 2000] and Centro de Investigación Científica y de Educación Superior de Ensenada (CICESE). Data from 1993 to 2002 are archived at the Southern California Earthquake Center (SCEC) and University Navstar Consortium (UNAVCO) database servers, whereas the most recent data since 2002 are stored at CICESE. The GPS campaign survey for measuring the surface displacements after the El Mayor-Cucapah earthquake was conducted by teams from CICESE, University of California, San Diego (UCSD) and University of California, Riverside (UCR). The first postseismic survey was conducted over a time interval of one day to one week after the mainshock. In addition to making observations at preexisting benchmarks, we also obtained GPS positions at new sites installed to the west of the earthquake rupture in the Laguna Salada basin. Some GPS stations were occupied in a semi-continuous mode for the first 1-2 months after the event to characterize the very earliest postseismic transients.

We processed all the available data from northern Baja California with the GAMIT/GLOBK processing package, version 10.35 [*Herring et al.*, 2008]. In the first step the package uses double-difference phase data between GPS satellites and stations to solve for station coordinates, atmospheric zenith delays and integer ambiguities for a full UTC day, in a loosely constrained solution covariance matrix. Next, GLOBK software is used to estimate velocities, by combining the loosely constrained solution with the IGS global solution from Scripps Orbit and Permanent Array Center (SOPAC) for all surveyed sites in the ITRF2005 reference frame.

Interseismic position corrections were made using our pre-seismic velocity field for northern Baja California extrapolated over time after the earthquake. This extrapolated position was then subtracted from the new position to obtain the coseismic and postseismic displacements. We applied the same procedure to the permanent GPS stations located north of the international border, in California, using online solutions from SOPAC with their

corresponding pre-seismic velocity corrections at each site; these permanent GPS data provided azimuthal coverage north of the earthquake rupture.

Synthetic Aperture Radar (SAR) data used in this study were collected by Envisat and ALOS satellites. The data are archived at the Western North America InSAR Consortium (WInSAR) at UNAVCO and at the Alaska Satellite Facility (ASF). We processed interferometric pairs from Envisat tracks 306 and 356, and ALOS track 211, across the El Mayor-Cucapah rupture spanning the first 5 months after the event, using the software package ROI_PAC version 3.0.1 [*Rosen et al.*, 2004] to create line-of-sight (LOS) displacement maps. The topographic contribution to the interferometric phase was removed using a digital elevation model with 90 m pixel resolution from the Shuttle Radar Topography Mission [*Farr et al.,* 2007]. This elevation model was augmented by a 5-m resolution Light Detection and Ranging (LIDAR) grid of the Sierra Cucapah provided by Instituto Nacional de Estadistica y Geografia (INEGI), Mexico.

3. Postseismic Deformation Transients

To isolate the postseismic motion, the coseismic offsets and the preseismic secular trend were removed from each GPS station record. Another coseismic offset caused by a major aftershock on June 15, 2010 (Mw 5.7) on the Ocotillo fault northwest of the main rupture, was also removed from the continuous GPS data. The postseismic displacement components, $D(x)$, can be fitted either with an exponential decay function [*Shen et al.,* 1994] (e.g., expected in case of linear viscoelastic rheology), logarithmic function [*Savage and Svarc*, 2009], and/or a rate-strengthening friction law [*Barbot et al*., 2009] (e.g., expected in case of afterslip). These functional relationships can be defined as follows:

$$D(x) = D_{pos}\left[1 - exp\left(-\frac{t}{\tau}\right)\right], \quad (1)$$

$$D(x) = Cln\left(1+\frac{t}{\tau}\right), \tag{2}$$

$$D(x) = A\left[1-\frac{2}{k}coth^{-1}\left(exp\left(\frac{t}{\tau}\right)coth\frac{k}{2}\right)\right], \tag{3}$$

where x is the displacement component, τ is the characteristic relaxation decay time (in days), D_{pos} is the permanent postseismic displacement, C is an amplitude constant for the logarithm function, A is an amplitude constant which relates the stress drop and the stiffness of a slip patch and k is a dimensionless ratio which controls the degree of nonlinearity during slip evolution. We performed a nonlinear curve fitting for each of these functions using an iterative procedure that minimizes the reduced chi-square value.

The time dependence of the observed near-field horizontal displacements during the first ~750 days after the mainshock (Figure 2), shows a gradually decelerating motion in the direction of coseismic offsets. Overall, the logarithmic and hyperbolic cotangent functions fit the data better than the exponential function. The characteristic decay time for the east and north components of sites in the near-field (MXCT, LASA, PUAS and LPUR) are: $\tau_{exp} = 66 \pm 9$ days (exponential decay), $\tau_{ln} = 20 \pm 3$ days (logarithmic decay) and $\tau_{coth} = 258 \pm 22$ days (hyperbolic cotangent decay, for *k*=3.0). These characteristic relaxation times for postseismic displacements are comparable to those estimated for recent earthquakes in southern California, such as the 1992 Landers earthquake, $\tau_{exp} = 84 \pm 23$ days [*Savage and Svarc*, 1997], and 1999 Hector Mine earthquake, τ_{exp} from 110 to 177 days [*Jacobs et al.*, 2002] and $\tau_{ln} = 26 \pm 8$ days [*Savage and Svarc*, 2009]. Overall, τ estimates increase with distance from the earthquake rupture. From τ_{exp} one can infer an effective viscosity of the ductile substrate, assuming a linear visco-elastic rheology [e.g., *Feigl and Thatcher*, 2006];

for a crustal shear modulus $\mu = 33GPa$, $\eta \sim 2x10^{17} Pa \cdot s$, similar to the "transient" viscosity inferred by *Pollitz et al.* [2012] based on the far-field continuous GPS measurements of deformation following the El Mayor-Cucapah earthquake.

In addition to GPS measurements, which provide millimeter-scale accuracy and 3-component but spatially sparse displacement vectors, we analyzed InSAR data that provide LOS projection of the displacement field with spatial resolution up to tens of meters and a centimeter-scale accuracy. We processed data from Envisat and ALOS satellites, acquired from both ascending and descending orbits, from April 13 to September 3, 2010 (Table 1). For example, the interferometric pairs shown in Figure 3, are from: April 13 to August 31 for Envisat ascending track 306 (hereafter 'Ea3'), April 16 to September 3 for Envisat descending track 356 (hereafter 'Ed3'), and April 17 to September 2 for ALOS ascending track 211 (hereafter 'Aa3'). In general, LOS displacement maps exhibit a good correlation of the radar phase. However, the Envisat Ea3 interferogram shows significant de-correlation of the radar phase in the Mexicali Valley, primarily due to agricultural activities. This de-correlation is less severe in the ALOS Aa3 interferogram, due to a longer radar wavelength of ALOS.

In order to qualitatively evaluate the near-field deformation features, we made five profiles perpendicular to the fault trace (thin black lines in Figure 3). These profiles (Figure 4) span three different time periods (Table 1) and reveal common features that can be attributed to postseismic deformation rather than to the atmospheric noise. In profile A-A', at the Paso Superior fault, just north of the rupture, Envisat LOS postseismic displacements are characterized by 3-4 cm of subsidence located primarily on the hanging wall side of the fault. Subsidence reaches a maximum within 1 km of the fault trace and diminishes at distances of 3-4 km (Figure 4a and 4b). Profile B-B' extends across the Laguna Salada basin and the northern tip of the Borrego fault. Two distinct features can be identified: a broad

ground subsidence in Laguna Salada, and a very narrow trough (~1 km wide), both displaying ~4 cm of subsidence (Figure 4c and 4d). On the other hand, a broader deformation pattern of the same amplitude is observed for profile C-C' across the Pescadores fault (Figure 4e and 4f). A projection of the 3-component GPS displacements onto LOS shows a good agreement between the GPS and InSAR data. For example, for the LPUR site, located on the northeast side of C-C', comparison of the respective LOS displacements yields: -2.7±.1.2 cm (GPS) vs. -3.8 cm (Aa3), and -2.1±1.2 cm (GPS) vs. -2.2 cm (Ea3).

Ed2, Ea2 and Aa2 interferometric pairs for the A-A', B-B' and C-C' profiles in the Sierra domain show significant decrease in LOS velocities (red lines at Figure 4a to 4f) in ~70 days (two orbital satellite periods) after the earthquake, suggesting a rapid postseismic relaxation process near the fault, which is similar to the characteristic relaxation decay time inferred from the GPS observations.

In the southwest half of profile D-D' significant uplift is observed, whereas in the northeast, differential subsidence reaches up to 10 cm in the Mexicali Valley (Figure 4g). Profile E-E' indicates subsidence of 5-6 cm, southwest of the southernmost Indiviso fault in the Colorado River delta (Figure 4h). In contrast to the rapid postseismic relaxation in the Sierra domain, LOS displacements in the Delta domain appear to be steady during the five months of observations.

4.- Postseismic Deformation Model

Large earthquakes are typically followed by postseismic deformation in response to coseismic stress changes. Several physical mechanisms have been invoked to explain the observed deformation transients: afterslip [*Marone et al.*, 1991; *Perfettini and Avouac*, 2004; *Barbot et al.*, 2009], poroelastic rebound of fluid saturated crust [*Peltzer et al.*, 1998; *Jonsson et al.*, 2003; *Fialko* 2004a], viscoelastic relaxation in the lower crust and upper mantle

[*Pollitz et al.*, 2001], and volume changes in the fault zone [*Massonnet et al.*, 1996; *Jacobs et al.*, 2002, *Fielding et al.*, 2009], among others. In this section, we explore which mechanisms can describe the early near-field postseismic deformation following the El Mayor-Cucapah earthquake.

Postseismic poroelastic rebound is expected to occur in the upper crust due to percolation of pore fluids driven by coseismic changes in the pore pressure. The timescales of poroelastic rebound depend on the effective permeability of rocks, and might vary from months [e.g., *Jonsson et al.*, 2003] to years [e.g., *Fialko*, 2004a]. In some instances, no evidence of poroelastic rebound on these time scales was found [e.g., *Barbot et al.*, 2008].

To evaluate the potential contribution of poroelastic effects [e.g. *Segall*, 2010; *Barbot and Fialko*, 2010] in the case of the El Mayor-Cucapah earthquake, we differenced the predicted coseismic displacement fields assuming drained and undrained Poisson's ratios of υ_d=0.21 and υ_u=0.25, respectively, resulting in a Poisson ratio difference of 0.04 [*Frez and Gonzalez*, 1991].

The static coseismic slip distribution model from *Fialko et al.*, [2010; http://igppweb.ucsd.edu/~fialko/baja.html; Figure 6a and fault geometry in Table 2], was used to calculate the fully relaxed poroelastic response. The coseismic model was obtained from inversion of all available space geodetic data, including SAR imagery from Envisat and ALOS satellites, optical imagery from SPOT-5 satellite, and continuous and campaign GPS data, assuming that the earthquake rupture can be approximated by rectangular dislocations in a homogeneous elastic half-space [e.g. *Fialko* 2004b]. The fault geometry is composed of seven rectangular segments (Table 2 and Figure 6a) that follow the main rupture trace at the surface, but have variable dip angles, as suggested by data inversions. Five of the segments are located in the Sierra domain and the other two in the Delta domain. From the northwest to the southeast along the main rupture: segment 1 corresponds to the Paso Superior fault,

segment 2 corresponds to the Paso Inferior accommodation zone (PIAZ), the northern half of segment 3 corresponds to the Borrego fault and the southern half to La Puerta accommodation zone (PAZ), segment 4 and half of segment 5 correspond to the Pescadores fault, all of these segments are dipping to the east; the southern half of segment 5 and segments 6 and 7 correspond to the Delta domain region, the latter two segments are dipping to the west.

While both the time scale and the amplitude of the poroelastic rebound are poorly constrained, the predicted fully relaxed poroelastic response likely serves as an upper bound on potentially observable poroelastic effects over the early postseismic epoch. A visual comparison of the InSAR data (Figure 3) and the poroelastic model predictions (Figure 5), as well as the GPS data and model predictions (Figure 5d), shows that the poroelastic rebound could account for some fraction of the observed postseismic signal: east of the Paso Superior fault (segment one) west of the PIAZ (segment two), the southeastern end of the Pescadores fault (segment five), and the southeastern end of the Indiviso fault (segment seven). However, in general the predicted poroelastic displacements are small compared to the observed signal. Therefore, we conclude that the near-field postseismic deformation is dominated by a different mechanism. We subtracted the predicted fully relaxed poroelastic displacements from the InSAR and GPS data in our subsequent analysis.

Next, we performed joint inversions of LOS and GPS observations spanning the first 5 months after the event for the postseismic slip distribution, using forward models based on rectangular dislocations in a homogeneous elastic half-space [*Okada,* 1985]. We used the fault geometry from the coseismic rupture model by *Fialko et al.* [2010]. LOS observations (Figure 3) are down-sampled to reduce the number of data points to 16 by 16 bin size (~500m by 500m pixels). Correspondingly, we used GPS observations spanning 9-150 days of postseismic displacement. After several simulations, we established that the relative weights

of 1.0 for the LOS data, and 0.3 for the GPS data allow one to fit each dataset relatively well, without substantially degrading the quality of fit to the other. The postseismic afterslip distribution on the fault segments was found iteratively, following a least squares minimization procedure, which relates slip on individual fault patches to surface displacements from LOS and GPS data. The regularization condition used in our inversion minimizes slip variations between adjacent slip patches. Details of the inversion formalism can be found in *Fialko* [2004b].

We did a number of inversions with increasing degrees of freedom, to determinate which features are required by the data. We began by restricting the fault slip to be pure strike-slip, followed by a combination of strike- and dip-slip components. Such a combination is suggested by the fact that the earthquake had an oblique coseismic slip, with nearly equal contributions of strike-slip and dip-slip components [*Fialko et al.*, 2010; *Wei et al.*, 2011a]. Our results indicate that the data are most consistent with the right-lateral strike-slip component. The direction of the dip-slip component was not constrained and was allowed to vary along the fault [e.g., *Simons et al*., 2002; *Jacobs et al.*, 2002]. A smoothness constraint was imposed on both slip components, based on the compromise between the quality of fit to the data and the model roughness.

The joint inversion of the InSAR and GPS data resulted in a postseismic displacement field consistent with the coseismic slip mechanism. We point out that although the combined strike- and dip-slip (i.e., variable rake) model was able to explain much of the data, it failed to account for several pronounced features such as the fault-zone subsidence [e.g., *Jacobs et al.*, 2002; *Fielding et al.*, 2009]. To account for these features, we increased the number of degrees of freedom to include fault-normal displacements, i.e. volume changes in the fault zone. The root mean square (RMS) misfit between the data and the model is 1.6 cm for the strike-slip and dip-slip component model, and 1.1 cm for the combined strike-slip, dip-slip,

and fault normal displacement component model (see supplementary analysis).

The three-component afterslip model yields an improvement in the RMS misfit of ~40% compared to the two-component model. It is expected that the RMS misfit value should decrease as the number of degrees of freedom increases. We can estimate the standard deviation of the InSAR LOS displacements by projecting the standard deviation of GPS data onto the radar LOS [*Hanssen,* 2001; e.g. Figure 4e and 4f]. The result is 1.1 cm, which should be considered as a lower bound. Therefore we conclude that the fault-normal component is required by the data and supported by the estimated errors. The inferred sense of fault-normal displacements indicates contraction, possibly due to recovery of co-seismic dilatancy in the fault zone.

The best-fit model is able to explain the near-field observations reasonably well. In particular, fault-normal contraction reproduces the subsidence observed west of the PIAZ and the northern tip of the Borrego fault, east of the Pescadores fault and west of the Indiviso fault (Figure 6-b and Figure 7). East of the Paso Superior fault (segment one), subsidence is controlled by ~20 cm of oblique shallow (2-5 km depth) afterslip. Fault-normal contraction is located along the shallower part of the PIAZ (segment two) and the Borrego fault (segment three). The source of postseismic deformation is ~10 cm of contraction, which contributes to the subsidence observed in the Laguna Salada basin, and ~8 cm of contraction located in a very narrow fractured zone at the northern tip of the Borrego fault. On the Pescadores fault (segments four and five) the postseismic slip is localized on the down-dip peripheral area of relatively high coseismic slip, with ~12 cm of fault-normal contraction at shallow depth, where segments four and five intersect. At this location the earthquake caused a prominent steam vent at the surface [*Fletcher et al.*, 2013]. On the Indiviso fault, the fault-normal contraction inferred from our analysis is along a zone of distributed fracturing and widespread liquefaction. The contraction is located at ~5 km and ~10 km depth, extending to

the surface where segments six and seven meet, and in the southernmost tip of segment seven, respectively. It is worth mentioning that an afterslip model with strike- and dip-slip components can only approximately fit the data over the entire Delta domain, but the inclusion of fault-normal contraction results in a better fit very near the fault trace.

The geodetic moment release may be estimated by integrating slip over the fault area, and multiplying by the crustal shear modulus. The value appropriate for fractured crustal rocks is likely between 10-33 GPa [e.g., *Hamiel et al.*, 2006; *Cochran et al.*, 2009]. The postseismic transient geodetic moment from April 13 (9 days after the main shock) to September 3, 2010, is between ~2.8×10^{18}N·m. and ~8.1×10^{18}N·m. In comparison, the cumulative seismic moment released by aftershocks located within 3 km from the fault trace (M>3.0, RESNOM catalog; http://resnom.cicese.mx/) over the same time period is ~3.5×10^{17}N·m. Thus, we find the ratio of geodetic to seismic moment release to be between 8 and 23, i.e. postseismic deformation is predominantly aseismic.

5. Discussion

Our analysis of the campaign GPS observations during the first ~750 days after the El Mayor-Cucapah earthquake (Figure 2), suggests that the near-field early postseismic deformation is consistent with stress-driven afterslip [e.g., *Savage and Svarc*, 2009; *Barbot et al*., 2009].

In particular, we derived kinematic afterslip models by inverting GPS and InSAR observations spanning the first 5 months after the earthquake, using analytic solutions for a dislocation in a homogeneous elastic half-space [*Okada*, 1985]. The observed displacements have been corrected for a possible poroelastic contribution assuming the difference between the drained and undrained Poisson ratios of ~0.04. The best-fit model (Figure 6) shows postseismic fault slip of ~10-40 cm located mainly on the periphery of the main coseismic

slip patches, in particular at the northern tip of the Paso Superior fault segment, on the Pescadores fault, and along the Delta domain on the Indiviso fault, where it is located near the surface and at depth, with an intervening "locked" zone in the middle of the seismogenic layer. The aftershock activity appears to concentrate on the periphery of both coseismic slip and afterslip, i.e. in areas that experienced the largest coseismic stress increases and the largest postseismic stressing rates. The estimated geodetic moment is an order of magnitude larger than the cumulative seismic moment released by aftershocks, indicating that most of afterslip occurred aseismically, consistent with previous results for other earthquakes [e.g. *Shen et al.*, 1994; *Jacobs et al.*, 2002; *Fialko*, 2004a; *Barbot et al*., 2009].

The afterslip model allowing for strike- and dip-slip components alone has RMS value of 1.6 cm; in order to get a better fit to the observations, we included in the inversion a fault-normal (i.e., opening or closure) displacement component. This reduces the RMS value to 1.1 cm (see Supplemental Materials). The predominant sense of fault-normal motion is contraction, which better explains the near-field deformation compared to the afterslip model with no volume changes. The inferred volume reduction could be due to closure of cracks and fissures produced by the seismic rupture, and represent postseismic healing of the earthquake-induced damage [e.g., *Jacobs et al.*, 2002; *Feigl and Thatcher*, 2006; *Fielding et al*., 2009]. Note that depending on the depth of the inferred volume changes, the model can produce vertical displacements with opposite polarity at the surface: a relative uplift of the fault zone in case of a fault zone collapse at depth [*Massonet et al.*, 1996], and a relative subsidence in case of a shallow fault zone collapse that extends to the surface [e.g., *Jacobs et al*., 2002].

In this study, the inferred fault-normal contraction is generally shallow and correlated to areas that experienced maximum coseismic slip (Figure 7b). In the Sierra domain, at the PIAZ and the northern part of the Borrego fault, contraction coincides with a prominent left

stepover in the surface rupture. Left stepovers in right lateral fault systems form restraining (compressive) bends; however, in the case of the PIAZ, geological evidence and differential LIDAR suggest that coseismic slip is predominantly extensional despite the left stepping geometry due to the overall oblique dextral-normal kinematics of the rupture [*Fletcher et al.* 2013; *Oskin et al.*, 2012]. Nonetheless, the fault zone contraction at this left stepping segment of the rupture suggested by our model may still reflect the restraining bend effect [*e.g. Jacobs et al.*, 2002; *Fielding et al.*, 2009]. The latter may be also responsible for subsidence in the Laguna Salada basin. Also, at the Pescadores fault, where right-lateral displacements up to 3.0 m and down-to-east vertical displacements up to 2.0 m were measured [*Fletcher et al.*, 2013], the contraction contributes partly to the subsidence on the east side of the fault (Figure S1). In the Delta domain, the predicted poroelastic displacements are substantially smaller and of opposite sign compared to the observations (Figure 3 and Figure 5), ruling out this mechanism as a cause of the observed deformation in that area. Fault-normal contraction inferred at the central and southern sections of the Indiviso fault partly cause subsidence on the west side of the rupture (Figure S1). We note that a large contraction zone located near the southernmost tip of the earthquake rupture (Figure 6b) may be a model artifact if subsidence along the Indiviso fault (fault segment 7, see Figure 7) is caused by some other process such as compaction of poorly consolidated sediments in the Colorado River Delta [*Nelson et al.*, 2013].

Our preferred afterslip model reproduces the observed postseismic displacements in the near-field reasonably well (Figures 6 and 7). It is worth emphasizing that the GPS data were assigned relatively small weights compared to the InSAR data, as the latter provide more details on the spatial distribution of postseismic deformation in the near-field. GPS data in the northeastern quadrant of the rupture show uplift, indicating a possible contribution from poroelastic rebound (Figure 5). Overall, the afterslip model is able to explain

postseismic displacements in the near field (within ~25 km from the rupture) reasonably well (Figure 8b). In the far-field, the postseismic model tends to under-predict the observed GPS displacements (Figure 8). Also, there is a substantial fault-normal component of postseismic GPS velocities north of the rupture (Figure 8a). Such a pattern may be evidence for an additional deformation mechanism, most likely viscoelastic relaxation in the lower crust and upper mantle [e.g., *Hearn*, 2003; *Fialko*, 2004a; *Pollitz et al.*, 2012]. Unfortunately, failure of the ALOS and Envisat satellites resulted in termination of the InSAR time series at the end of year 2010, restricting our ability to evaluate relative contributions of all potential mechanisms of postseismic deformation due to the El Mayor-Cucapah earthquake. Continued observations of the on-going transient, including data from the permanent GPS networks, as well as campaign surveys of the existing benchmarks in the near-field of the earthquake rupture will extend the GPS time series and help further refine models of postseismic deformation.

6. Conclusions

The postseismic displacements observed using GPS during the first two years after the El Mayor-Cucapah earthquake are consistent with afterslip on the earthquake rupture plane, with possible contributions from poro-elastic and visco-elastic relaxation. Characteristic decay times for surface velocities are: 66 ± 9 days for the exponential decay, 20 ± 3 days for the logarithmic decay, and 258 ± 22 days for the analytic rate-strengthening friction law.

Our preferred afterslip model, obtained through joint inversion of GPS and InSAR data from April to September 2010, indicates that most of the afterslip occurred on the periphery of the main coseismic slip patches. Aftershocks occurred preferentially in between the areas of high coseismic slip and afterslip, possibly delineating a boundary between the velocity-weakening and velocity-strengthening parts of the fault. While postseismic deformation can be in general adequately fit by oblique slip on the fault, a better fit in several

areas, including the Laguna Salada basin at the Paso Inferior accommodation zone, the northern tip bend of the Borrego fault, and the Pescadores fault, can be achieved by allowing fault-normal contraction at shallow depth. The estimated geodetic moment is an order of magnitude larger than the cumulative seismic moment of aftershocks during the same period. In the far field (at distances greater than ~25 km from the earthquake rupture) the afterslip model tends to under-predict surface displacements, suggesting a contribution from viscoelastic relaxation in the ductile substrate [e.g., *Pollitz et al.,* 2012].

Acknowledgments

We thank the Associate Editor and two anonymous reviewers for their thorough and thoughtful reviews of this manuscript. This work was partially financially supported by CONACyT projects 81463 and 133042, NSF (EAR-1053627), SCEC projects 11075, 12204, 08098, 09065 and NASA (NNX09AD12G). Envisat data are copyright 2010 ESA and were obtained from WinSAR archive. ALOS data are copyright JAXA and were obtained from the Alaska Satellite Facility Level 1 Data Pool. Regional seismic data were provided by RESNOM. Most of the figures were generated by Generic Mapping Tool (GMT) software [*Wessel et al.,* 2013]. We thank the support and interest from Distrito de Riego XIV S.R.L. de C.V. during the GPS campaigns.

References

Barbot S., Hamiel Y., and Fialko Y. Space geodetic investigation of the coseismic and postseismic deformation due to the 2003 Mw 7.2 Altai earthquake: Implications for the local lithospheric rheology. *J. Geophys Res.* 113, B03,403. 2008.

Barbot S., Fialko Y., and Bock Y. Postseismic deformation due to the Mw 6.0 2004 Parkfield earthquake: Stress-driven creep on fault with spatially variable rate-and-state friction parameters. *J. Geophys. Res.* 114, B07,405. 2009.

Barbot S. and Fialko Y. A unified continumm representation of the post-seismic relaxation mechanism: semi-analytic models of afterslip, poroelastic rebound and viscoelastic flow. *Geophys. J. Int.* 182, 1124-1140. 2010.

Bennett R. A., Rodi W. and Reilinger R. E. Global Positioning System constrains on fault slip rates in southern California and northern Baja Mexico. *J. Geophys. Res.* 101, 21943-21960. 1996.

Burgmann R. and Dresen G. Rheology of the lower crust and upper mantle: Evidence from rock mechanics, geodesy, and field observations. *Annu. Rev. Earth Planet. Sci*. 36, 531–567. 2008.

Castro R., Acosta J., Wong V., Perez-Vertti A., Mendoza A., and Inzunza L. Location of aftershocks of the 4 April 2010 Mw 7.2 El Mayor-Cucapah earthquake of Baja California, Mexico. *Bull. Seism. Soc. Am.* 101(6), 3072-3080. 2011.

Cochran E., Yong-Gang L., Shearer P., Barbot S., Fialko Y., and Vidale J. Seismic and geodetic evidence of extensive, long-lived fault damage zones. *Geology* 37, 315-318. 2009.

Dixon T., Farina F., DeMets C., Suarez-Vidal F., Fletcher J., Marquez-Azua B., Miller M., Sanchez O., and Umhoefer P. New kinematic models for Pacific-North America motion from 3 Ma to present, II: Evidence for a "Baja California shear zone". *Geophys. Res. Lett.* 27, 3961-3964. 2000.

Farr T.G., Rosen P.A., Caro E., Crippen R., Duren R., Hensley S., Kobrick M., Paller M., Rodriguez E., Roth L., Seal D., Shaffer S., Shimada J., Umland J., Werner M., Oskin M., Burbank D. and Alsdorf D. The shuttle radar topography mission. *Rev. Geophys.* 45(2). 2007.

Feigl K. and Thatcher W. Geodetic observations of post-seismic transients in the context of the earthquake deformation cycle. C.R. *Geoscience* 338, 1012-1028. 2006.

Fialko, Y. Evidence of fluid-filled upper crust from observations of postseismic deformation due to the 1992 Mw 7.3 Landers earthquake. *J. Geophys. Res.* 109, B08,401. 2004a.

Fialko Y. Probing the mechanical properties of seismically active crust with space geodesy: Study the co-seismic deformation due to the 1992 Mw 7.3 Landers (southern California) earthquake. *J. Geophys. Res.* 109, B03,307. 2004b.

Fialko Y., Gonzalez A., Gonzalez J., Barbot S., Leprince S., Sandwell D., and Agnew D. Static rupture model of the 2010 Mw 7.2 El Mayor-Cucapah earthquake from ALOS,

ENVISAT, SPOT and GPS data. American Geophysical Union. Fall Meeting, Abstract T53B-2125, San Francisco, California. 2010. http://igppweb.ucsd.edu/~fialko/baja.html. Last accessed October 2013.

Fielding E., Lundgren P., Burgmann R., and Funning G. Shallow fault-zone dilatancy recovery after the 2003 Bam earthquake in Iran. *Nature Letters* 458, 64-68. 2009.

Fielding E. J., Wei S., Leprince S., Sladen A., Simons M., Avouac J., Briggs R. W., Hudnut K. W., Helmberger D. V., Hensley S., Hauksson E., Gonzalez-Garcia J. J., Herring T., and Akciz, S. O. Kinematic fault slip model from joint inversion of teleseismic, GPS, InSAR and subpixel-correlation measurements of the 2010 El Mayor-Cucapah earthquake and postseismic deformation. American Geophysical Union. Fall Meeting, Abstract T51E-08, San Francisco, California. 2010.

Fletcher J. and Spelz R. Patterns of Quaternary deformation and rupture propagation associated with an active low-angle normal fault, Laguna Salada, Mexico: Evidence of a rolling hinge?. *Geosphere* 5, 385-407. 2009.

Fletcher J., Teran O., Rockwell T., Oskin M., Hudnut K., Mueller K., Ronald S., Akcis S., Masana E., Faneros G., Fielding E., Leprince S., Morellan A., Stock J., Lynch D., Elliot A., Gold P., Liu-Zeng J., Gonzalez-Ortega A., Hinojosa-Corona A., and Gonzalez-Garcia J. Assembly of large earthquake from a complex fault system: Surface rupture kinematics of the April 4, 2010 El Mayor-Cucapah Mw7.2 earthquake. Submitted to *Geosphere*. 2013.

Frez J. and Gonzalez J.J. Crustal structure and seismotectonics of northern Baja California. *In*

The Gulf and Peninsular Province of the Californias, J. P. Dauphin and B.R. Simoneit Eds. AAPG Memoir 47. Chap. 15. Tulsa, Oklahoma. 1991.

Hamiel, Y., O. Katz, V. Lyakhovsky, Z. Reches, and Y. Fialko, Stable and unstable damage evolution in rocks with implications to fracturing of granite. *Geophys. J. Int*. 167, 1005-1016. 2006.

Hanssen R. F. Radar Interferometry - Data Interpretation and Error Analysis (Remote Sensing and Digital Image Processing, Volume 2) (v. 2). Springer. 328 pp. 2001.

Hauksson E., Stock J., Hutton K., Wenzheng Y., Vidal-Villegas J.A. and Kanamori H. The 2010 Mw 7.2 El Mayor-Cucapah earthquake sequence, Baja California, Mexico and southernmost California, USA: Active seismotectonics along the Mexican pacific margin. *Pure Appl. Geophys.* 168, 1255-1277. 2010.

Hearn, E.H. What can GPS Tell us About the Dynamics of Postseismic Deformation?. *Geophys. J. Int.*, 155, 753-777. 2003.

Hearn E., McClusky S., Ergintav S., and Reilinger R. Izmit earthquake postseismic deformation and dynamics of the north Anatolian fault zone. *J. Geophys. Res*. 114, B08,405. 2009.

Herring T., King R., and McClusky S. Introduction to GAMIT/GLOBK, report, Mass. Inst. of Technol., Cambridge. 2008.

Jacobs A., Sandwell D., Fialko Y., and Sichoix L. The 1999 (Mw 7.1) Hector Mine, California, earthquake: Near-field postseismic deformation from ERS interferometry. *Bull. Seism. Soc. Am.* 92(4), 1433-1442. 2002.

Jonsson S., Segall P., Pedersen R., and Bjornsson G. Post-earthquake ground movements correlated to pore-pressure transients. *Nature* 424, 179-183. 2003.

Marone C., Scholz C., and Bilham R. On the mechanics of earthquake afterslip. *J. Geophys. Res.* 96, B5, 8441-8452. 1991.

Massonnet D., Thatcher W., and Vadon H. Detection of postseismic fault-zone collapse following the Landers earthquake. *Nature* 382, 612-616. 1996.

Nelson S., Fielding E., Zamora-Arroyo F., and Flessa K. Delta dynamics: Effects of a major earthquake, tides, and river flows on Ciénega de Santa Clara and the Colorado River Delta, Mexico. *Ecological Engineering*. 59, 144-153. 2013.

Okada, Y. Surface deformation due to shear and tensile faults in a half-space. *Bull. Seism. Soc. Am.* 75, 1135–1154. 1985.

Oskin M., Arrowsmith R., Hinojosa-Corona A., Elliot A., Fletcher J., Fielding E., Gold P., Gonzalez-Garcia J., Hudnut K., Liu-Zeng L., and Teran O. Near-field deformation from the El Mayor-Cucapah earthquake revealed by differential LIDAR. *Science* 335, 702-705. 2012.

Peltzer G., Rosen P., Rogez F., and Hudnut K. Poroelastic rebound along the Landers 1992

earthquake surface rupture. *J. Geophys. Res.* 103, 30131-30145. 1998.

Perfettini H., and Avouac J. Postseismic relaxation driven by brittle creep: A possible mechanism to reconcile geodetic measurements and the decay rate of aftershocks, application to the Chi-Chi earthquake, Taiwan. *J. Geophys. Res.* 109, B02,304. 2004.

Pollitz F., Wicks C., and Thatcher W. Mantle flow beneath a continental strike-slip fault: Postseismic deformation after the 1999 Hector Mine earthquake. *Science* 293, 1814-1818. 2001.

Pollitz F., Burgmann R., and Thatcher W. Illumination of the rheological mantle heterogeneity by the M7.2 El Mayor-Cucapah earthquake. *Geochem. Geophys. Geosyst.* 13(6). 2012.

Rosen, P., Hensley S., Peltzer G., and Simons M. Updated repeat orbit interferometry package released. *Eos Trans. AGU*, 85(5), 47. 2004.

Rymer M.J., Treiman J.A., Kendrick K.J., Lienkaemper J.J., Weldon R.J., Bilham R., Wei M., Fielding E.J., Hernandez J.L., Olson B.P.E., Irvine P.J., Knepprath N., Sickler R.R., Tong X., and Siem M.E. Triggered surface slips in southern California associated with the 2010 El Mayor-Cucapah, Baja California, Mexico, earthquake. U.S. Geological Survey Open-File report 2010-1333 and California Geological Survey Special Report 221, 62 p. 2011.

Savage J., and Svarc J. Postseismic deformation associated with the 1992 Mw=7.3 Landers

earthquake, southern California. *J. Geophys. Res.* 102, 7565-7577. 1997.

Savage J., and Svarc J. Postseismic relaxation following the 1992 M7.3 Landers and 1999 M7.1 Hector Mine earthquakes, southern California. *J. Geophys. Res.* 114, B01,401. 2009.

Segall P. Earthquake and Volcano Deformation. Princeton University Press. 464 pp. 2010.

Shen Z., Jackson D., Feng Y., Cline M., Kim M., Fang P., and Bock Y. Postseismic deformation following the Landers earthquake, California, 28 June 1992. *Bull. Seism. Soc. Am.* 84(3), 780-791. 1994.

Simons M., Fialko Y., and Rivera L. Coseismic deformation from the 1999 Mw 7.1 Hector Mine, California, earthquake as inferred from InSAR and GPS observations. *Bull. Seism. Soc. Am.* 92(4), 1390-1402. 2002

Wei S., Fielding E., Leprince S., Sladen A., Avouac J., Helmberger D., Hauksson E., Chu R., Simmons M., Hudnut K., Herring T., and Briggs R. Superficial simplicity of the 2010 El Mayor-Cucapah earthquake of Baja California in Mexico. *Nature Geos*. 4, 615. 2011a.

Wei M., Sandwell D., Fialko Y., and Bilham R. Slip on faults in the Imperial Valley triggered by the 4 April 2010 Mw 7.2 El Mayor-Cucapah earthquake revealed by InSAR. *Geophys. Res. Lett.* 38, L01,308. 2011b.

Wessel P., Smith W. H. F., Scharroo R., Luis J. F., and Wobbe F. Generic Mapping Tools: Improved version released. *EOS Trans. AGU*, 94, 409. 2013.

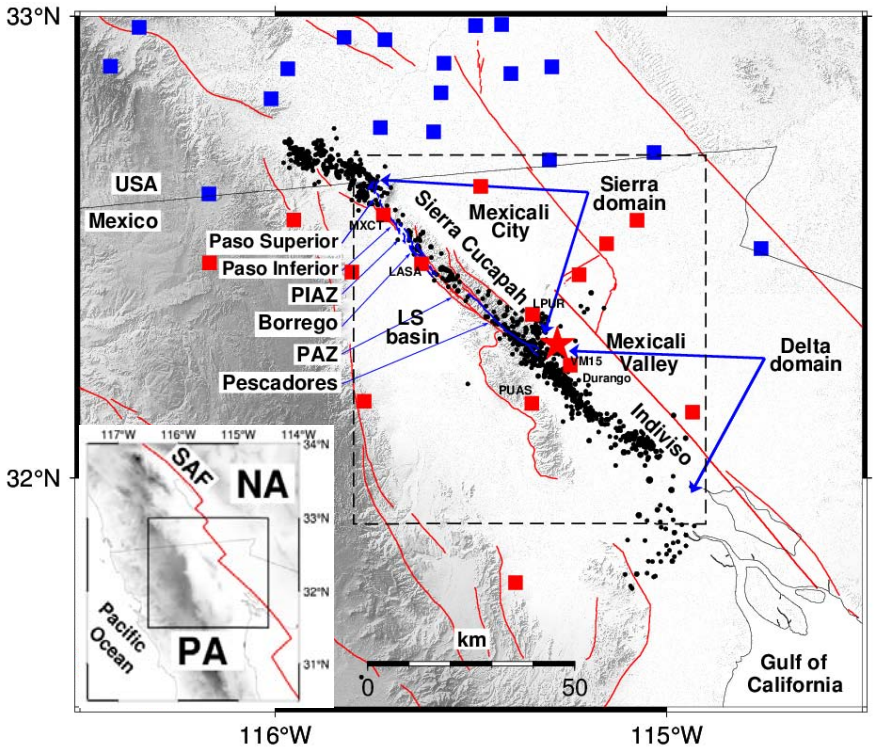

Figure 1: Map of the epicentral region of the El Mayor-Cucapah earthquake. The red star denotes the earthquake epicenter, black circles denote aftershocks that occurred during the first 5 months (RESNOM; http://resnom.cicese.mx/), red lines denote known active faults. Blue lines denote the surface trace of the 2010 rupture [Fletcher et. al. 2013]. Red and blue squares denote GPS sites in Mexico and USA, respectively. PIAZ: Paso Inferior Accommodation Zone, PAZ: Puerta Accommodation Zone, LS: Laguna Salada. Black dashed box outlines a region shown in Figures 3, 5 and 7. Inset illustrates a broader tectonic setting of the study area. NA: North American plate, PA: Pacific plate, SAF: San Andres Fault system.

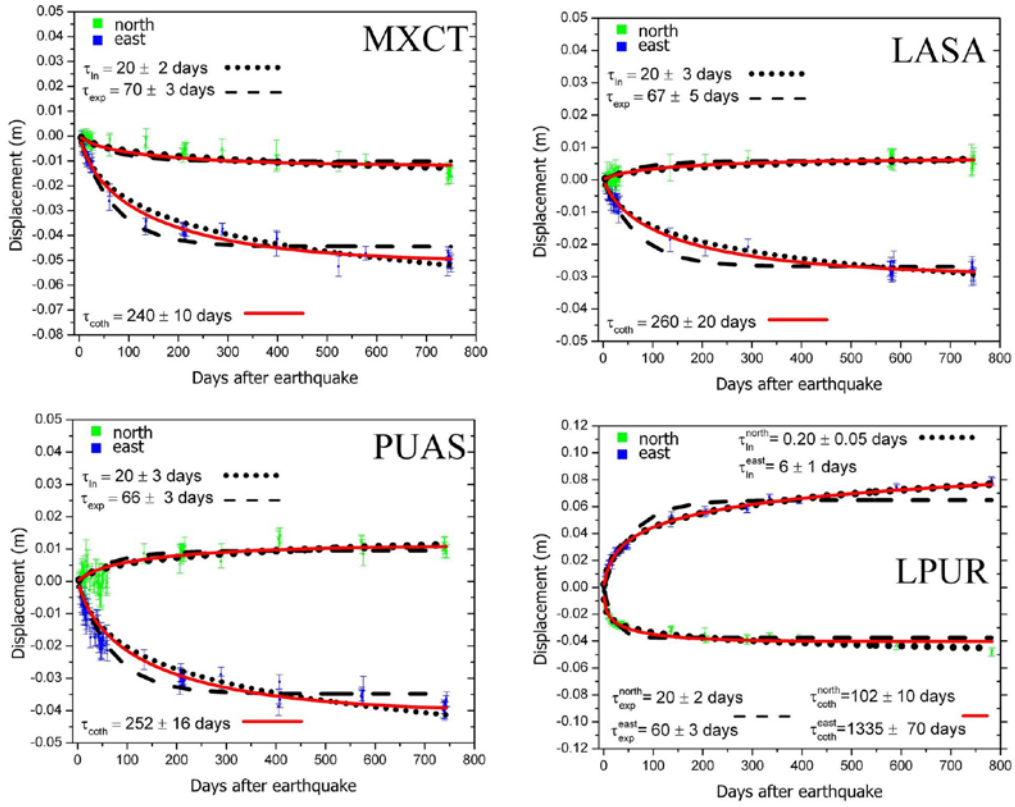

Figure 2: Daily GPS positions for the four sites closest to the earthquake rupture. The North and East components of the displacement vector are denoted by the green and blue symbols, respectively. The best-fitting exponential, logarithmic and hyperbolic cotangent functions are indicated by the black dashed, black dotted, and solid red lines, respectively. Also shown are the corresponding relaxation times (τ).

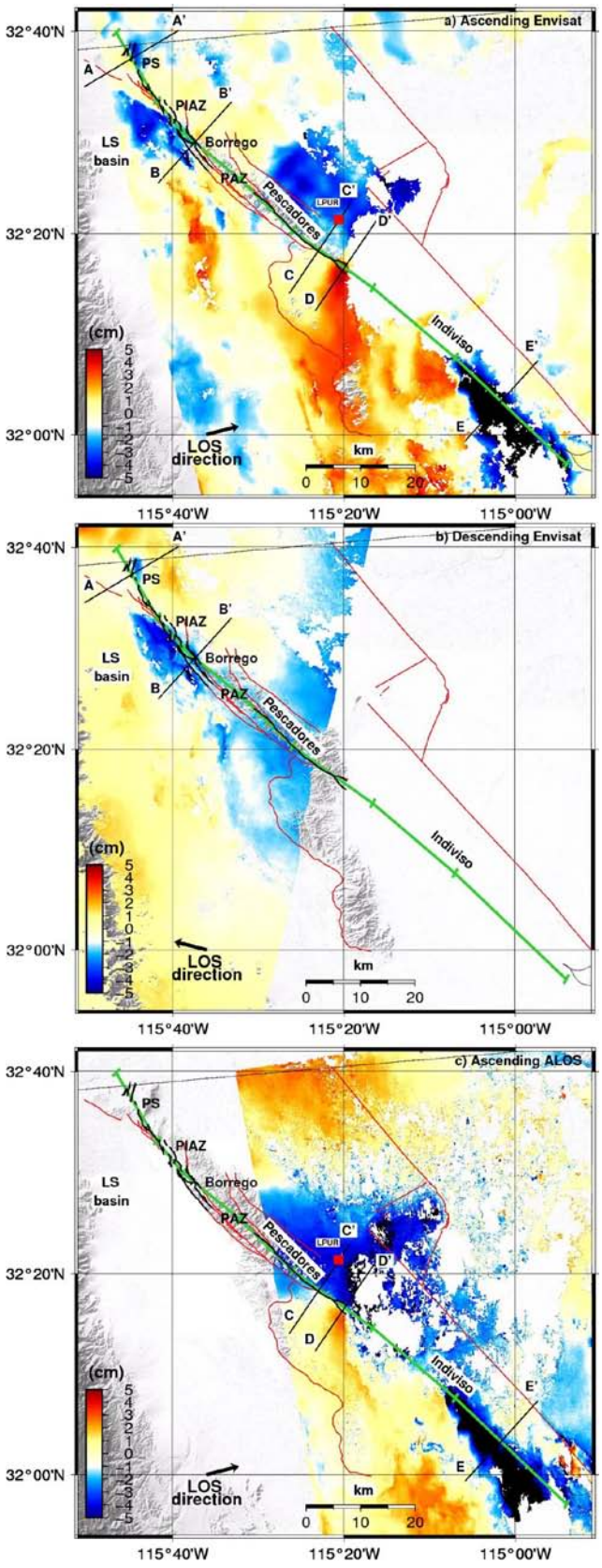

Figure 3: Radar interferograms spanning a time period of ~5 months after the earthquake: a) Ea3, April 13 to August 31, b) Ed3, April 16 to September 3, and c) Aa3,

April 17 to September 2, 2010 (see Table 1). Colors denote surface displacements along the satellite LOS, positive toward the satellite. Straight black lines denote fault-perpendicular profiles shown in Figure 4. Green line denotes the trace of the fault model used in our study (Table 2). Red square denotes the location of GPS site LPUR. PS: Paso Superior. Other notation is the same as in Figure 1.

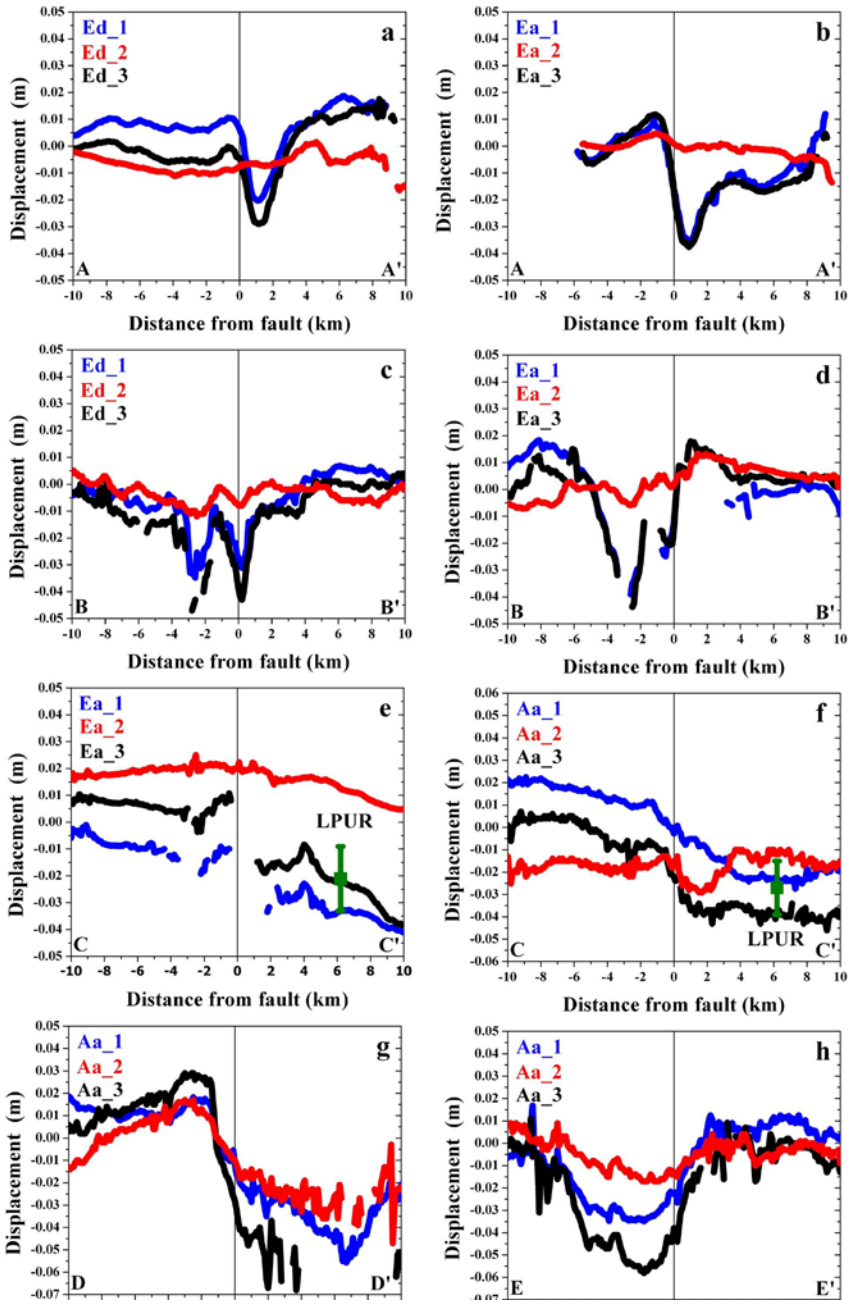

Figure 4: Profiles across the fault trace (see Figure 3) in zones of enhanced near-field deformation, for different time periods (see Table 1). Positive LOS displacements correspond to ground motion toward the satellite.

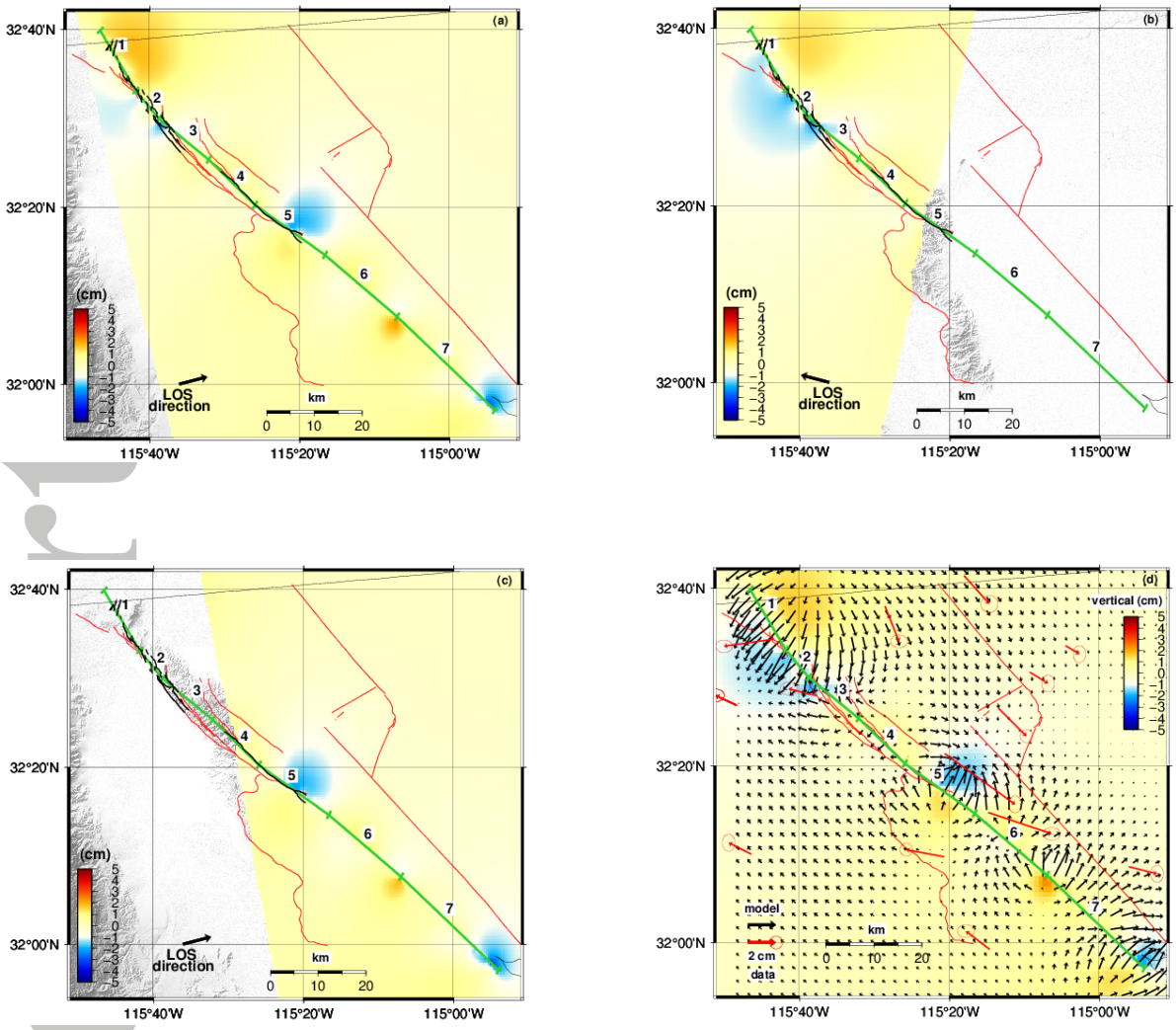

Figure 5: Predictions of the poroelastic rebound model. a) - c) Surface displacements projected onto the satellite LOS corresponding to interferograms shown in Figure 3 (Ea3, Ed3, Aa3). d) Horizontal (black arrows) and vertical (color) displacements due to poroelastic rebound. Observed horizontal GPS displacements are shown for comparison (red arrows). Numbers correspond to fault segments of the model (Table 2). Notation is the same as in Figure 3.

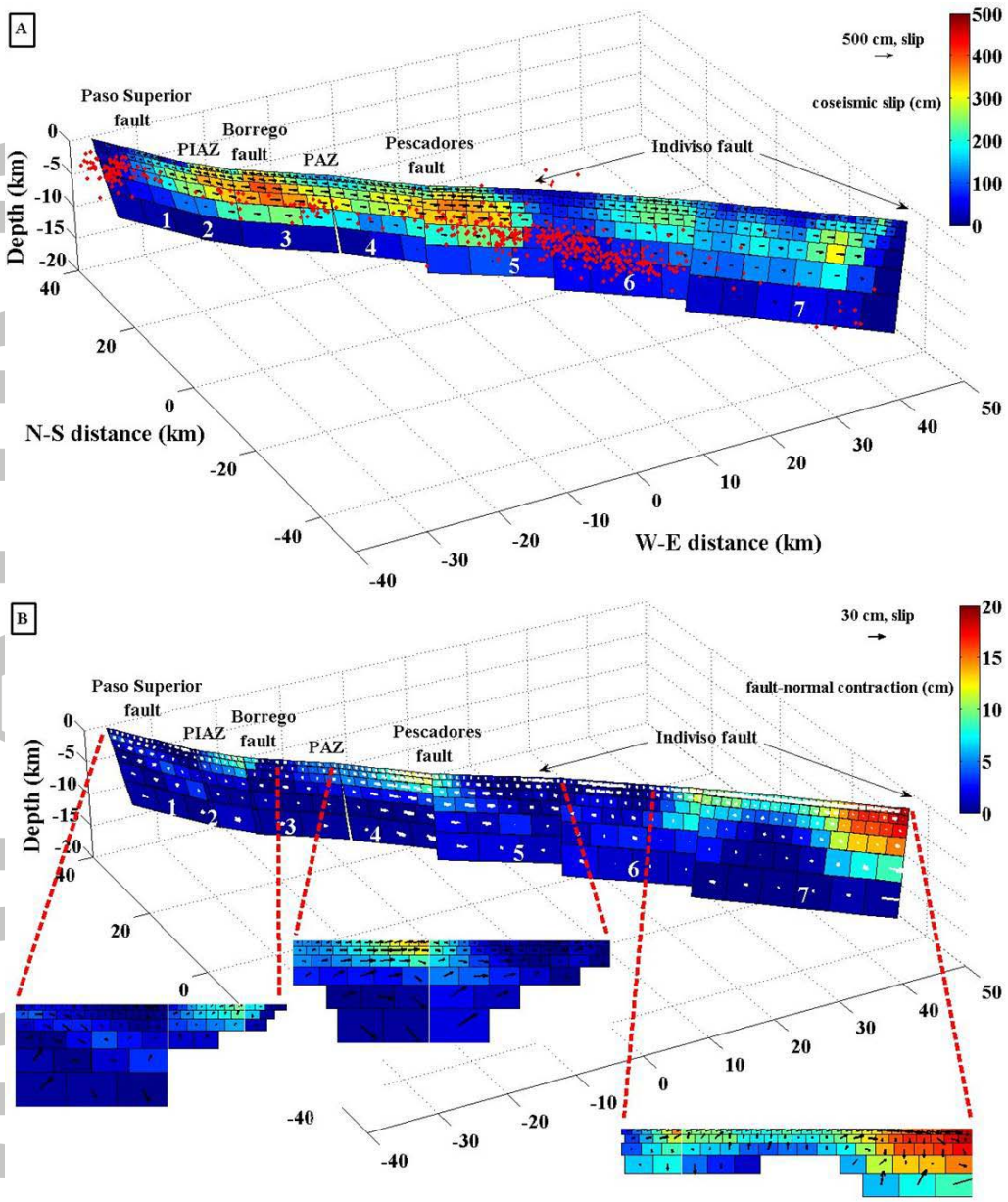

Figure 6: A) Finite coseismic slip model from *Fialko et. al.*, [2010]. Colors denote the amplitude of slip. Red circles denote aftershocks during the first 5 months. B) Best-fitting postseismic model. Colors denote the amplitude of fault-normal displacements (contraction is positive), and arrows denote the distribution of afterslip.

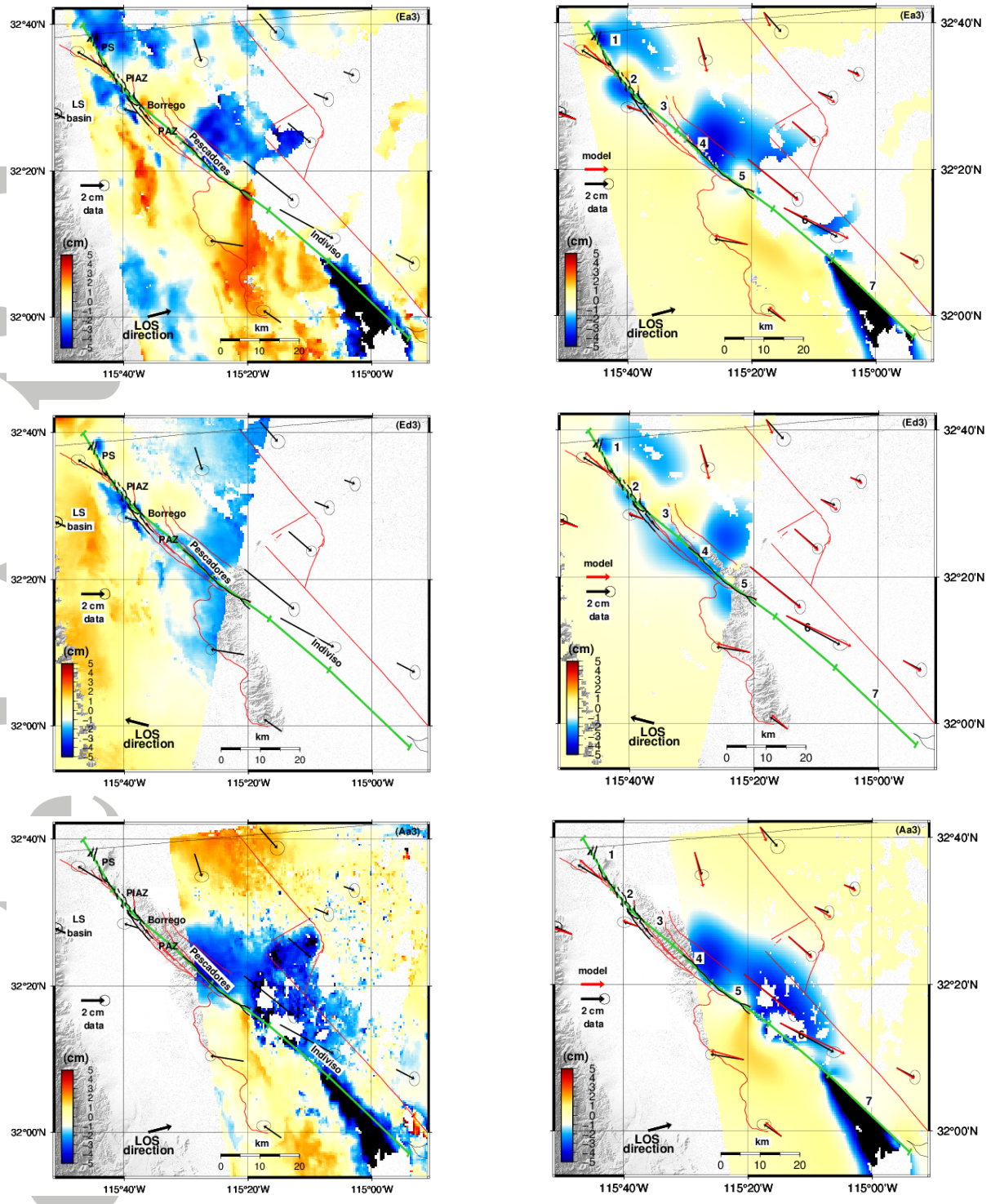

Figure 7: Left panels: InSAR (color) and GPS (black arrows) data corrected for the presumed poroelastic deformation. Right panels: predictions of the best-fitting afterslip model. Notation is the same as in Figure 3.

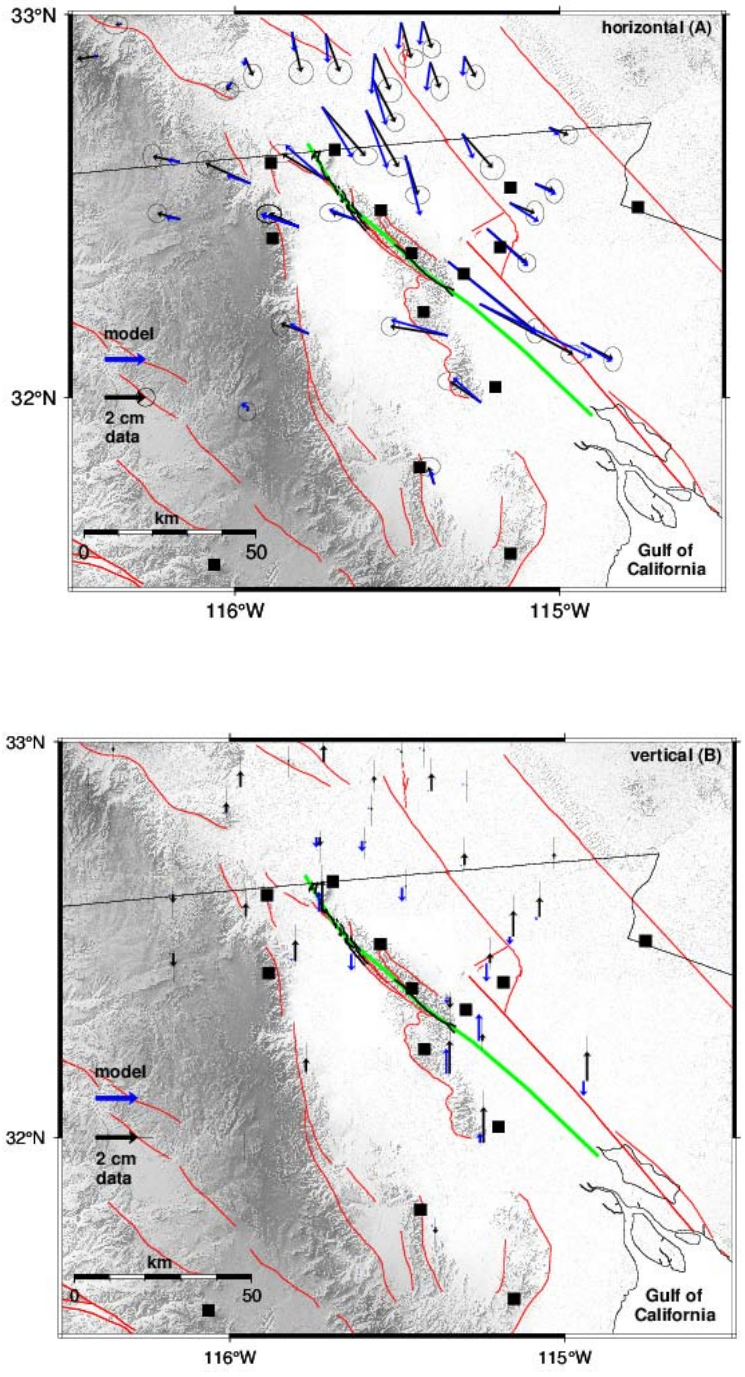

Figure 8: Observed GPS displacements over the time period of 5 months following the earthquake (black arrows) and the best-fitting model predictions (blue arrows). The presumed poroelastic contribution was subtracted from the data. Black squares denote permanent GPS sites installed after the earthquake (UNAVCO/Eartscope-PBO and Caltech Tectonic Observatory). Notation is the same as in Figure 3.

Table 1: Interferometric pairs used in this study.

Satellite	Tracks	Dates	nomenclature
ENVISAT	356	16 April – 25 June	Ed1
		25 June – 3 September	Ed2
		16 April – 3 September	Ed3
ENVISAT	306	13 April – 22 June	Ea1
		22 June – 31 August	Ea2
		13 April – 31 August	Ea3
ALOS	211	17 April – 2 June	Aa1
		2 june – 2 September	Aa2
		17 April – 2 September	Aa3

Table 2: Fault geometry and geographical locations at segment centers from *Fialko et. al.*, [2010].

	Fault segments						
	1	2	3	4	5	6	7
W Longitude	115.74	115.67	115.59	115.48	115.35	115.20	115.01
N Latitude	32.61	32.53	32.46	32.38	32.29	32.19	32.04
Strike (deg)	N31°W	N40°W	N52°W	N46°W	N56°W	N50°W	N47°W
Dip (deg)	71°NE	71°NE	71°NE	71°NE	79°NE	89°SW	59°SW
Length (km)	15.20	7.58	13.48	13.55	17.95	19.94	28.77